ADVANCED FUNCTIONAL MATERIALS
www.afm-journal.de

Catalyst-Free Synthesis and Characterization of Metastable Boron Carbide Nanowires

By *Aruna Velamakanni, K. J. Ganesh, Yanwu Zhu, Paulo J. Ferreira,* and *Rodney S. Ruoff**

Catalyst-free growth of boron carbide nanowires is achieved by pyrolysis of diborane and methane at 650–750 °C and around 500 mTorr in a quartz tube furnace. Electron-diffraction analysis using a novel diffraction-scanning transmission electron microscopy (D-STEM) technique indicates that the crystalline nanowires are single-crystal orthorhombic boron carbide. TEM images show that the nanowires are covered by a 1–3 nm thick amorphous layer of carbon. Elemental analysis by electron energy loss spectroscopy (EELS) shows only boron and carbon while energy-dispersive X-ray spectroscopy (EDX) and X-ray photoelectron spectroscopy (XPS) show the presence of oxygen as well as boron and carbon.

1. Introduction

Boron carbide is an extremely hard ceramic material with a hardness value of 9.3 on the Mohs scale. Its other properties include a low density 2.52 g cm^{-3}, outstanding elastic modulus 540 GPa (slightly dependent on crystalline direction),[1] chemical and temperature stability, and good neutron-absorption cross section.[2] The high hardness and low density of boron carbide have resulted in the development of lightweight armor ceramic composites.[3] Boron carbide also finds application in the aerospace industry as a rocket propellant.[4,5]

Bulk boron carbide has a low fracture toughness which makes it unsuitable for various applications where mechanical strength is important.[6] To overcome this problem, there has been some work done in recent years to synthesize boron carbide nanostructures. Conventional techniques such as reduction of boron trioxide for the production of boron carbide are complex and expensive because of its high melting point. Hence, most research has been focused on chemical vapor deposition (CVD) to synthesize boron carbide at low processing temperatures.

Boron carbides with a rhombohedral crystal structure are most stable. Common stoichiometries include $B_{13}C_2$, $B_{12}C_3$, and B_4C, and some that are close to $B_{12}C_3$.[7,8] Other crystal structures such as tetragonal ($B_{50}C_2$, $B_{50}C$, $B_{48}C_3$, $B_{51}C$, $B_{49}C_3$)[9] and orthorhombic (B_8C)[7,10] have also been confirmed, but these structures are metastable.[7] The latter phases are more difficult to synthesize than the stable rhombohedral phases, and their physical properties are also not well known.[10–12]

Various methods have been reported for the synthesis of bulk, thin films as well as nanostructures of boron carbide.[13] Thin films of boron carbide have been synthesized via direct ion-beam deposition[14] and plasma-enhanced chemical vapor deposition (PECVD) from boranes.[15,16] A low-temperature synthesis of bulk boron carbide by the reaction of boric acid and polyvinyl alcohol[17] has also been reported. The major advantage of CVD synthesis over other methods is the better control over the processing conditions, which eventually affect the final properties of the deposit. Several gas mixtures such as BCl_3–CH_4–H_2–Ar,[18,19] B_2H_6–CH_4–H_2,[20] and B_2H_6–CH_4–$B(CH_3)_3$[21] have been used to synthesize various phases of boron carbide.

A patent[22] has been issued to K. Kourtakis on the synthesis of boron carbide nanorods with a B/C ratio of 8 to 1. Their method employed heating boron oxide in the presence of a reagent "comprising nickel and boron" supported on carbon at a temperature of 900–1300 °C. We here report on the catalyst-free growth of single-crystal boron carbide nanowires by pyrolysis of diborane and methane at significantly lower temperature (650–750 °C). Our method also employs different starting materials and has fewer steps in the synthesis.

Veprek et al.[20] in 1989 and Kuenzli et al.[21] in 1998 were some of the other groups who used a similar combination of precursor gases (B_2H_6+CH_4+H_2; other synthesis conditions being different). In the present work, the synthesized boron carbide has a different morphology (nanowires instead of films) and has been assigned the orthorhombic structure, as will be discussed in the later sections.

2. Results and Discussions

2.1. Synthesis

The experiments for the growth of boron carbide nanowires were carried out in a home-built low-pressure chemical vapor deposition (LPCVD) furnace system, whereby the temperature

[*] Prof. R. S. Ruoff, Prof. P. J. Ferreira, Dr. A. Velamakanni, Dr. Y. Zhu
Department of Mechanical Engineering and Texas Materials Institute
University of Texas at Austin
1 University Station, C 2200, Austin, Texas, 78712 (USA)
E-mail: r.ruoff@mail.utexas.edu
K. J. Ganesh
Materials Science and Engineering Program
University of Texas at Austin
1 University Station, C 2200, Austin, Texas, 78712 (USA)

DOI: 10.1002/adfm.200901146

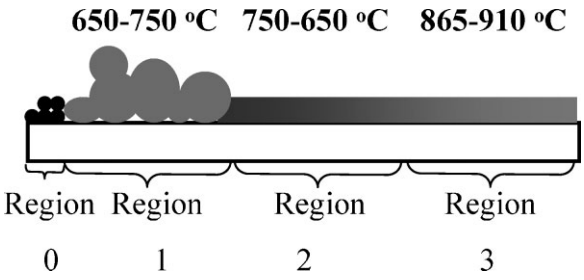

Figure 1. Schematic of the substrate after a typical deposition showing the various morphologies in the 4 cm region according to the different temperature zones. (Regions not to scale.)

gradient throughout the furnace was measured before deposition (see experimental). The details of this system have been mentioned elsewhere.[23]

After deposition several morphologies were observed along the length of the 4 cm substrate used. A schematic representation of the different regions is depicted in Figure 1. The first region of around 0.5 cm in length (<650 °C) contained a gray deposit. Diborane pyrolyzes between 600–800 °C to yield pure boron and also pyrolytic boranes.[24] Hence at temperatures below 650 °C, only this material was deposited (''region 0''). Dark-gray ''spherical deposits'' (visible to the eye) were randomly found in the next region of around 1 cm in length of the substrate (650–750 °C, ''region 1''). The subsequent region of around 1 cm in length (750–865 °C, ''region 2'') consisted of dark-brown deposits. Light-brown deposits were observed in the last region of around 1.5 cm in length (865–910 °C, ''region 3''). The different temperature zones will be referred to by their region names henceforth. Oxygen-plasma cleaning had no impact on the morphology or nature of the nanostructures found in any of the regions. Substrates were also used without cleaning. The nanostructures presented here grew not only on the substrates but also on the boats used to load the substrates, as well as on the inside of the quartz tube, which were not plasma-cleaned before use. Characterization using various techniques (see below) on the nanostructures grown on the boats and on the inside walls of the quartz tube revealed that they had the same morphology as the ones grown on the substrates.

Deposits from all three regions mentioned above were characterized by scanning electron microscopy (SEM). The nanowires from the spherical deposits were studied in detail and are the focus of the present work. Transmission electron microscopy (TEM), electron energy loss spectroscopy (EELS), energy-dispersive X-ray spectroscopy (EDX), X-ray photoelectron spectroscopy (XPS), and Raman spectroscopy were used to better understand the crystal structure and growth mechanism of these nanowires.

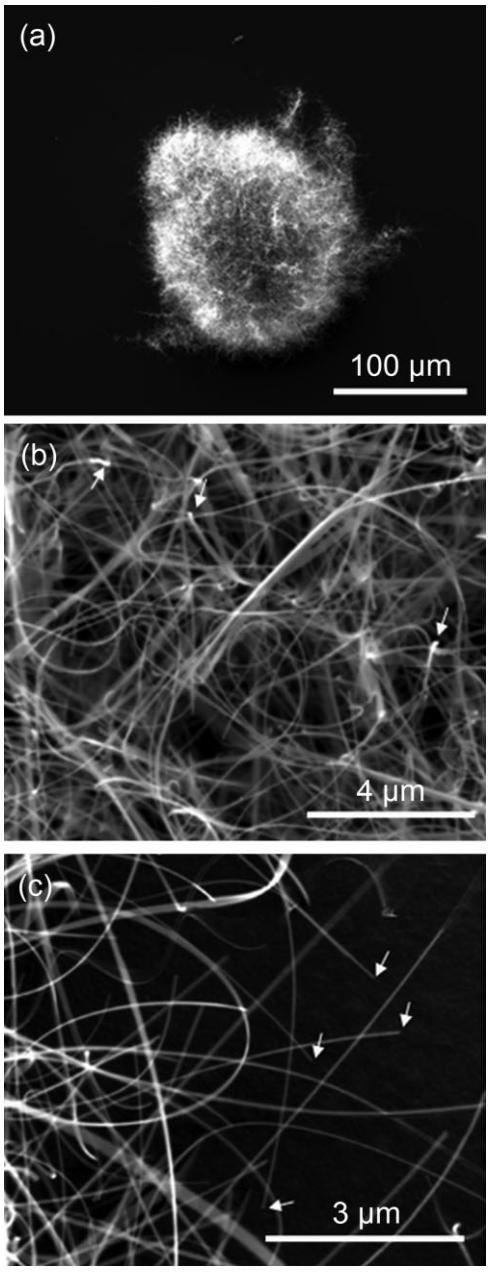

Figure 2. SEM images of region 1 in Figure 1. a) Overall view of the ''spherical deposits''. Higher magnification images are shown in (b) and (c). b) Nanowires and nanobelts are evident. The white arrows indicate a bright spot which could be related to folding of the nanowires/nanobelts. c) Ends of nanowires (white arrows) show no catalyst particles at the tips.

2.2. Scanning Electron Microscopy (SEM) Analysis

The spherical deposits were around 150 μm to 1 mm in diameter depending upon the growth time (45 min–2.5 h). Figure 2a shows a low-magnification image of one of the spherical deposits grown for nearly 45 min. Figure 2b takes a closer look at the spherical deposits which reveals that they consist of nanostructures with different morphologies. Most of the nanostructures have diameters of 15 nm ±5 nm referred to as smaller nanowires. The larger nanowires were 50 nm ±5 nm in diameter. The length of the nanowires in region 1 was a few tens of micrometers. Neither the diameters nor the lengths of these nanowires were dependent on the growth time (i.e., whether a minimum growth time of 45 minutes or a maximum growth time of 2.5 h was used, the

lengths and distribution of diameters of the nanowires remained the same). The spherical deposits obtained after 45 minutes of growth had a smaller diameter (ca. 150 μm), were sparsely distributed in the region where they grew, and also looked less dense when viewed by SEM. The growth for 2.5 h resulted in a larger number of spherical deposits (that is, distributed over a larger area) that were larger in size (up to 1 mm) and also were more dense when viewed by SEM. (The reason for the minimum time of 45 minutes is that for growth times less than this, it was difficult to find any deposits with the naked eye.) Some nanostructures also had a ribbon structure (or belt structure) with aspect ratios as measured for several such belts of about 4 to 5 (width/thickness). For example, measurement of several such nanobelts yielded thickness values of about 40 nm and widths of about 180 ± 10 nm. Figure 2c shows the ends of some nanowires and nanobelts. These structures showed no catalyst particle at their ends. Region 2 depicts nanostructures measuring around 50 nm in diameter and a few nanometers in length (Fig. 3). From region 2 to region 3, these structures evidently grew in length and became aligned parallel to the substrate. Towards region 3 the nanowires are seen to be much longer (ca. 2 μm) and entangled. The nanostructures in regions 2 and 3 do not show any differences in morphology with time of growth. No growth or deposits were observed beyond region 3.

2.3. Transmission Electron Microscopy (TEM) Analysis

Figure 4a shows a bright-field TEM image of the nanostructures obtained in regions 2 and 3. The diameter of these nanowires range from 10 to 50 nm, which is consistent with the SEM results (Fig. 2a and 2b). All nanowires (ca. 150 in number) observed by TEM had a crystalline core and an amorphous shell (Fig. 4b). The smaller nanowires (10–20 nm in diameter) have a thin 1–3 nm amorphous shell and the larger wires (ca. 50 nm) have a crystalline core of 20 nm and a much thicker amorphous shell (ca. 30 nm). The nanobelts with widths of around 150 nm were essentially consistent with the SEM results. No high-magnification images for the nanobelts were taken as they were not the subject of interest. The high-resolution TEM (HRTEM) image in Figure 4b shows the morphology of a typical nanowire of around 15 nm in diameter with a thick amorphous shell of around 3 nm. Figure 4c is a HRTEM image of a nanowire that is 50 nm in diameter depicting a thick amorphous carbon shell.

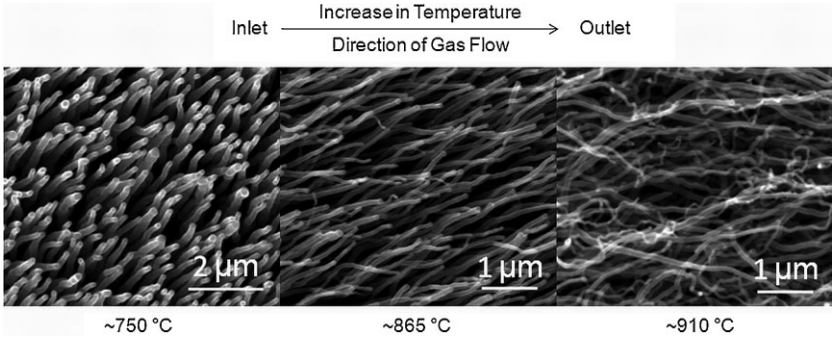

Figure 3. SEM images of regions 2 and 3 in Figure 1 of nanostructures varying in morphology according to the temperature gradient during deposition along the 2.5 cm long substrate. A change in the morphology of the nanostructures from lower to higher temperature is evident.

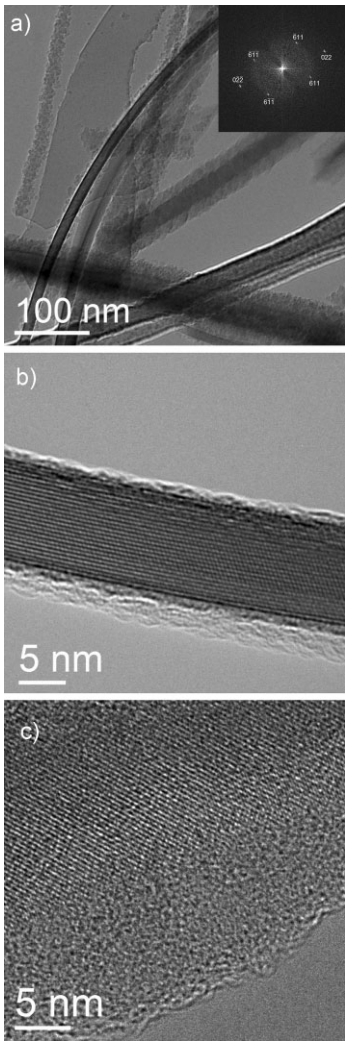

Figure 4. a) Bright-field TEM image of several nanostructures. b) Phase-contrast image of a nanowire ca. 18 nm in diameter. c) HRTEM image of the nanowire. Inset: fast Fourier transform (FFT) of the image.

2.3.1. Analysis by Electron Energy Loss Spectroscopy (EELS)

EELS and EDX (energy-dispersive X-ray spectroscopy) were performed in order to analyze the nanowire composition. As some of the larger nanowires (ca. 50 nm) had a very thick amorphous shell, EELS line scanning in a scanning transmission electron microscopy (STEM) configuration was employed to investigate the elemental distribution across the width of these nanowires (Fig. 5). Spectra were recorded without background subtraction from the center and edges. Spectra from the edges depicted a characteristic carbon K edge and a very small oxygen K edge. As the beam was translated towards the core, a small

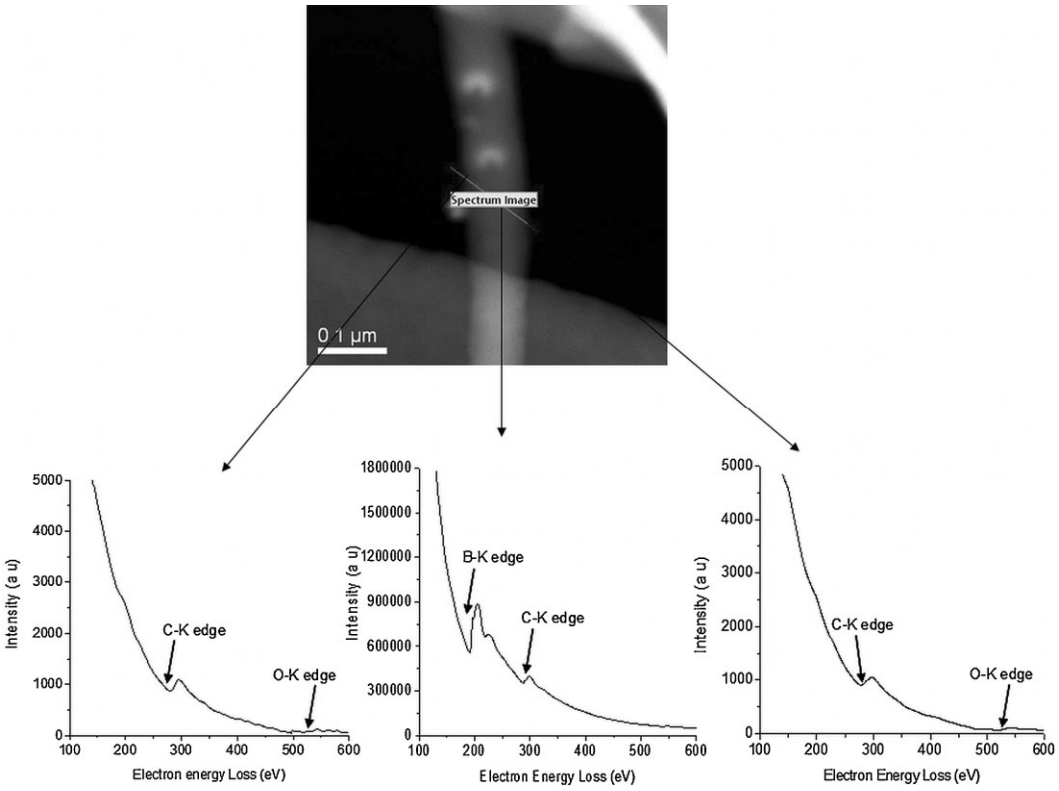

Figure 5. EELS spectra from the edges and center of a boron carbide nanowire showing that the amorphous coating contains only carbon and very little oxygen.

boron edge appeared which became more intense towards the center while the oxygen edge completely disappeared. The core showed only boron and carbon edges, no oxygen edge. The aforementioned pattern of elemental distribution was repeated when the beam moved towards the other edge. EDX analysis also detected boron, carbon, and a small amount of oxygen. The same sample was re-analyzed by EELS after it was exposed to air for several weeks and the same results were obtained. Quantitative analysis of the EELS spectrum of the core was performed on 19 nanowires from different specimens and each one of these showed a B to C ratio within the range of 7.95 ± 0.03, which is very close to the composition B_8C. These 19 nanowires were from specimens grown for different time durations. Quantitative EELS analysis was also performed on the amorphous carbon shell of several nanowires and the oxygen in the carbon shell ranging from 5–10 at %. The oxygen source could have been present both during the growth or may come from adsorbates, such as water, on the surface of the nanowires. It is difficult to quantitatively determine the oxygen that is (or may be) covalently bonded within the nanostructure as opposed to oxygen that is simply contained in molecules that are (or may be) adsorbed onto their surfaces.

Figure 6a represents a bright-field TEM image of the nanostructures from region 3. It shows amorphous wire-like structures of about 50 nm in diameter as confirmed by the electron-diffraction pattern in Figure 6b. Elemental analysis by EELS (Fig. 6c) shows only boron and carbon core-loss edges and no trace of oxygen. This is indicative of an amorphous material containing boron and carbon. Raman spectra of the same structures have been included in the supporting information.

2.3.2. D-STEM (Diffraction-Scanning Transmission Electron Microscopy) Analysis

To determine the crystal structure and stoichiometry of the material (in addition to EELS), a novel electron-diffraction technique called diffraction–scanning transmission electron microscopy (D-STEM)[25,26] was employed. This technique can obtain spot diffraction patterns from nanostructures as small as 3 nm. The details of this technique can be found elsewhere.[25,26] A single crystal Si[110] specimen was used to calibrate the camera length for D-STEM configuration. Figure 7a shows a representative bright-field STEM image of a nanowire ca. 50 nm in diameter. The 1–2 nm parallel probe was positioned on the wire at the center (labeled A) and the diffraction pattern taken (Fig. 7b).Indexing the patterns revealed the boron carbide to have an orthorhombic structure with lattice constants consistent with those reported in JCPDS file # 26-232: $a = 35.099$ Å; $b = 17.653$ Å; $c = 5.094$ Å. The results obtained from D-STEM analysis were found to be completely consistent with those obtained from Fast Fourier Transform (FFT) analysis (Fig. 4a, inset) of the high-resolution phase-contrast image shown in Fig. 4c. The same analysis was carried out on several nanowires and nanobelts and a series of electron-diffraction patterns were recorded and indexed. All of them reveal the presence of orthorhombic B_8C. B_8C is a metastable

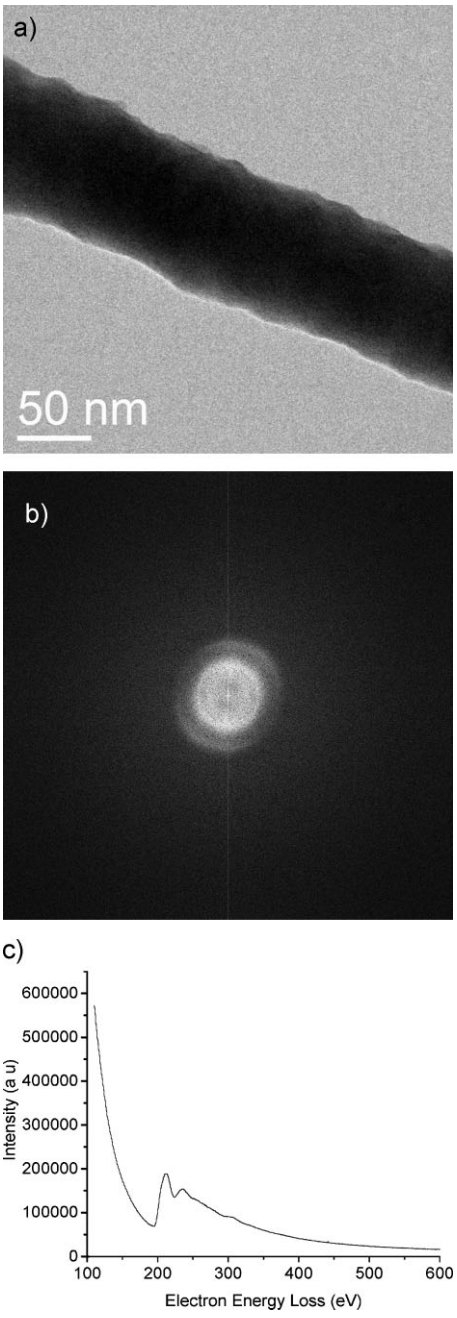

Figure 6. a) TEM image of nanowires grown at the highest temperature (region 3). b) Diffraction ring pattern showing that the nanowire is amorphous. c) EELS spectrum showing the boron and carbon edges.

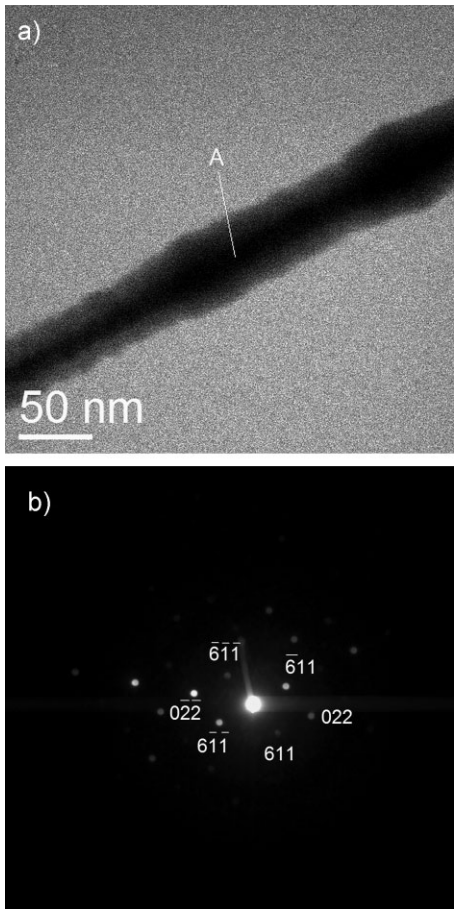

Figure 7. a) Bright field STEM image of a 50-nm diameter nanowire. b) Diffraction pattern using D-STEM from region A in (a) depicting a crystalline structure and near $01\bar{1}$ beam orientation.

phase of boron carbide and is not considered in B–C phase diagrams.[27]

It is well known that B_{12} icosahedra serve as structural elements in all boron carbides.[7] The residual B and C atoms occupy the large interstitial positions in the lattice and stabilize the structure.[7,28] Efforts to elucidate the crystal structure of the B_8C phase have been performed by Ploog et al.[12] However, the complete crystal structure of boron carbide with B_8C stoichiometry has not been conclusively determined.[7] It is stated that the stabilizing sub-units of $(B_{12})_4C_2$ are linked by additional C atoms in the *a*–*b* plane, whose locations could not be conclusively stated.

2.4. XPS (X-ray Photoelectron Spectroscopy) Analysis

Figure 8a shows the XPS survey-scan spectrum for binding energies from 0 to 1200 eV. In addition to the boron and carbon peaks, an oxygen peak was also detected. As discussed below, the source of oxygen could be from the nanowires but also in/on the underlying pyrolytic material. Figure 8b indicates the B 1s core-level spectrum that was fit to three components. The main component at 188.3 eV corresponds to the B–C bond, which is in good agreement with the reported values.[29–31] The component at 187.3 eV was assigned to the B–B bonds in boron carbide.[31] In the B 1s spectrum, the oxide-related species are observed above 190 eV. The small component at 190.2 eV has been assigned to the B–O bond. The presence of an O 1s feature at 533.0 eV in Figure 8d corresponds to a B–O bond that could be from the progressive oxidation of the surrounding pyrolytic boron[32] and not from the boron carbide nanowires, as no oxygen (corresponding to B–O) was detected in the nanowires using EELS. Figure 8c shows the C

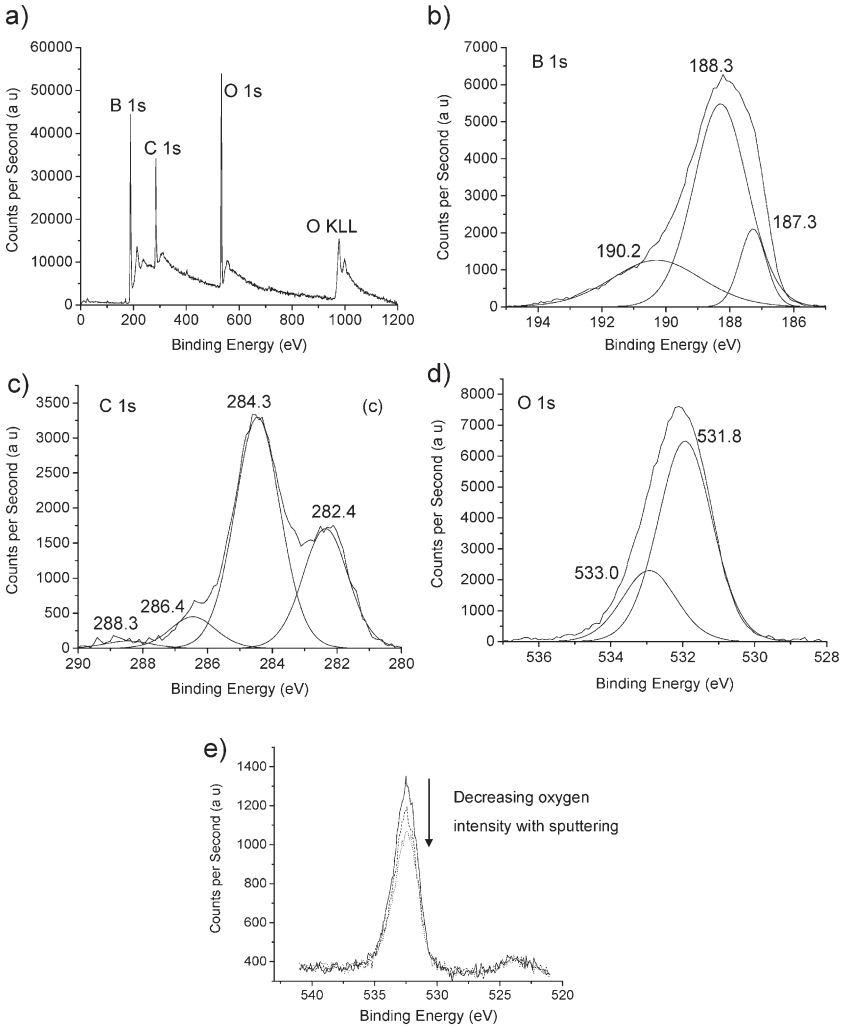

Figure 8. a) XPS survey scans showing the B 1s, C 1s, and O 1s peak of region 1 in Figure 1. XPS detailed scans: b) The B 1s peak was fit to three components at 187.3 eV, 188.3 eV, and 190.2; c) the C 1s peak was fit to four components at 282.4 eV, 286.4 eV, 284.3 eV, and 288.3 eV; d) the O 1s peak was fit to two components at 531.8 eV and 533.0 eV. The assigned bonding types are discussed in the text. e) Decrease in the oxygen peak intensity after sputtering with Ar^+ ions.

1s core-level spectrum. The C 1s peak was broad and asymmetric with a distinct shoulder. It was fit to four components. The component at 282.4 eV was assigned to the B−C bond. This C 1s spectrum component was associated with the B 1s component at 188.3 eV (Fig. 8a). The component at 284.3 eV was assigned to carbon contamination, as the material was exposed to ambient air for several weeks. The C 1s component at 286.4 eV was assigned to a C−O bond or C−OH bond.[33] A corresponding O 1s component associated with the C−O (or C−OH) bond appeared at 531.8 eV (Fig. 8d). The C 1s component at 288.3 eV (Fig. 8c) was assigned to a C=O linkage. The small oxygen K edge in the EELS spectrum probably corresponds to these oxidized functionalities of carbon. Ar^+ ion sputtering of these wires showed a decrease in the XPS oxygen peak intensity, indicating possible surface contamination related to exposure to ambient atmosphere upon transfer of the sample to the XPS chamber (Fig. 8e).

3. Growth Mechanism

Various mechanisms have been proposed for the growth of nanowires,[34,35] the most common being the vapor–liquid–solid (VLS) mechanism.[36] In this process, a second phase material, commonly referred to as a catalyst, forms a liquid droplet by itself or by alloying with the growth material and is typically located at the tip of the growing nanowire or nanotube.[37,38] This mechanism has been used to explain the growth of boron carbide nanowires where iron has been used as a catalyst.[35] In the present work, no catalyst was deliberately introduced in the system and, as a result, no catalyst particles were observed at the tips of these nanowires. Hence, the VLS mechanism can be ruled out as the growth mechanism in the present case. Several experiments were carried out in an attempt to determine the factors (such as flow rates of gases, reaction time, and type of substrate) that may influence the growth of these nanowires and, thus, explore the growth mechanism. As mentioned above, the growth of these nanowires was not really limited by the type of substrate (keeping the other parameters the same as mentioned above) as the nanowires were found to be growing all over the quartz tube, quartz or alumina boat, with or without SiO_2/Si substrates but within the same temperature zones. Growth runs were performed with different growth times between 20–150 min. Increasing the reaction time led to the formation of much larger spherical deposits with wider spatial coverage, but the morphologies of the individual nanowires remained the same. Growth of these nanowires was affected by the overall pressure in the furnace at the time of reaction. Lowering the pressure (to 300 mTorr) by turning off the Ar supply during the run resulted in no growth. On the other hand, increasing the pressure to 1.6 Torr, by increasing the flow rate of methane (160 sccm) also suppressed the growth. It was concluded that the best suitable pressure range for growth of these nanowires was 480–530 mTorr (at flow rates of 14.2 sccm for methane and 15 sccm for diborane and 15 sccm for Argon). The center reaction temperature was changed in increments of 25 °C (875–950 °C) and no significant changes were observed in the morphologies of these nanowires in the 650–750 °C temperature range. It can, thus, be concluded that the nanowires only grow in the 650–750 °C temperature regime.

In some of the runs, an oxygen scrubber was introduced upstream from the methane inlet, as it was detected by mass spectroscopy that the methane used contained very small amounts of oxygen. Surprisingly, no nanowires were grown in these cases when the other experimental parameters were kept the same. The same experiment without an oxygen scrubber did result in the growth of nanowires. Hence, we believe that the small amount of oxygen present in methane was, in fact, catalyzing the formation of

these nanowires. A possible mechanism for the growth of these boron carbide nanowires could be "oxygen-assisted growth" (see further).

The amorphous carbon shell also seemed to have played a role in confining the diameter of the crystalline core of the nanowires. It was observed that irrespective of the total diameter, which also includes the amorphous shell, the crystalline core was never more than 20 nm in diameter. The thickness of the amorphous carbon shell also increased with increasing nanowire diameter.

Pyrolysis of diborane produces many gas-phase products, including borane radicals such as BH_3, BH_2, and higher boranes such as B_4H_{10}, B_5H_{11}, B_5H_9, $B_{10}H_{14}$, etc. with the heavier species steadily increasing with a decrease in concentration of diborane; these have been detected by mass spectroscopy and could serve as the gaseous reactants.[39] Pyrolysis of methane has also been widely studied.[40,41] At temperatures below 700 °C, a small amount of oxygen can react with methane to form H_2O and carbon monoxide.[42] This water can in turn react with the gaseous borane radicals to form boric acid.[43] Boric acid can undergo dehydration at temperatures between 700 and 900 °C to generate boron oxide.[44] Boron oxide can then react with carbon monoxide to form boron carbide nanowires.[35]

In our LPCVD system, pyrolysis of B_2H_6 (for the center temperature of 950 °C used here) occurs extensively near the inlet of the reaction chamber. Thus, additional B-containing gaseous species are available in the inlet region. The extent of pyrolysis of methane also increases with an increase in temperature. Hence, few carbon species are available for reaction at the inlet (650–750 °C) because of the temperature gradient from the inlet to the center of the furnace.

We have also collected Raman spectra from the indicated regions (Fig. 1) (see also Supporting Information). However, we cannot conclusively determine whether the fraction of material that is present as B_8C nanowire cores inside of the C amorphous material is responsive to Raman spectroscopy or not.

4. Conclusions

Orthorhombic boron carbide (B_8C) nanowires and nanobelts with diameters ranging from 10–50 nm and 100–150 nm respectively have been grown by pyrolysis of diborane and methane. These nanowires grew in a temperature zone of 650–750 °C at 500 mTorr overall pressure. Amorphous boron carbide nanowires (up to 50 nm in diameter) of undetermined stoichiometry were also grown in the temperature zone of 750–910 °C. The presence of a small amount of oxygen was necessary for the growth of the nanowires. Raman data (Supporting information) strongly suggest that the boron carbide nanostructures that are formed at the inlet of the quartz tube in the lower temperature zone are composed of a boron-rich phase while those formed towards the center of the furnace in the high-temperature zone are composed of a carbon-rich phase. This method provides a facile procedure for growing nanowires of a metastable, orthorhombic boron carbide phase (B_8C), thus achieving kinetic vs. thermodynamic control. This paves the way for future work towards developing a deeper understanding of such less-known structures and their properties. We have included the Raman spectra in the hope that they will prove useful as a study of this metastable B_8C phase in the future.

5. Experimental

Synthesis: Silicon (Si) substrates with 290 nm-thick thermally grown SiO_2 (4 cm × 1 cm, University Wafer) were used for the experiments. They were ultrasonically cleaned using acetone and ethanol (Crest ultrasonic cleaner; 6 min), followed by oxygen-plasma cleaning (Plasma-862, Kurt J. Lesker; 3 min). The substrates were then loaded in an alumina or a quartz boat (for separate runs) and placed in the reaction chamber. The chamber was ramped up to 925 °C (center position temperature) in 60 min under a 15 sccm (standard cubic centimeter) continuous flow of argon (Airgas). Prior to the experiment, the furnace temperature was measured from the center to either side of the furnace, yielding the temperature gradient along the furnace. The temperature was measured at all locations along the length of the furnace, as well as at the inlet and exit. Subsequently, a gas mixture of 15 sccm diborane (5% hydrogen, Matheson Trigas) and 14.2 sccm methane (Airgas) was introduced into the chamber for 45 min. The total pressure for each run was 530 mTorr (for any particular run, the pressure was known to 3 significant figures). The gas flow was stopped after 45 min. and the power supply was turned off to let the furnace cool down to room temperature. The cooling process was carried out under Ar flowing at 5 sccm.

Scanning Electron Microscopy: SEM analysis was performed using a FEI Quanta Environmental SEM (ESEM). Substrates were directly loaded into the chamber with the deposits on them.

Transmission Electron Microscopy: Several deposits were scraped off the substrates from regions 1–3 and ultrasonically dispersed in ethanol (Crest ultrasonic cleaner, 6 min). A drop of this suspension was placed on a copper TEM grid covered with a lacey carbon film (Ted Pella 300 mesh). The morphology and crystal structure of the nanowires were investigated using a JEOL 2010F TEM/STEM (spherical aberration coefficient, $C_s = 0.5$mm) equipped with an ultrahigh resolution pole piece. An operating voltage of 200 kV was employed for imaging and diffraction purposes.

X-Ray Photoelectron Spectroscopy: XPS analysis was performed using a Kratos AXIS Ultra DLD XPS equipped with a 180° hemispherical energy analyzer to determine the chemical composition of the nanowires. Photoemission was stimulated by a monochromated Al Kα radiation (1486.6 eV) at an operating power of 150 W. It was operated in the analyzer mode at 80 eV for survey scans and 20 eV for detailed scans of core level lines. Binding energies were referenced to the C 1s binding energy set at 284.5 eV. The substrates with spherical deposits were directly loaded onto the sample bar for analysis.

Acknowledgements

This work was supported by NSF #0802247, *Fracture Mechanics of Nanowires and Nanostructures*, D. Kouris program manager. We thank Lew Rabenberg, H. Steinfink, and J.P. Zhou for insights pertaining to the electron-diffraction analysis, R. Piner, H. Celio, and H. Werheit for valuable insight and discussions. We also acknowledge the Center for Nanoscience and Technology and the Texas Materials Institute (TMI) at UT-Austin for use of the TEM and XPS user facilities, and the National Science Foundation (Grant # 0618242) for funding the X-ray Photoelectron Spectrometer used in this work. Supporting Information is available online from Wiley InterScience or from the author.

Received: June 26, 2009
Published online:

[1] V. Domnich, Y. Gogotsi, M. Trenary, T. Tanaka, *Appl. Phys. Lett.* **2002**, *81*, 3783.
[2] G. Goller, C. Toy, A. Tekin, C. K. Gupta, *High Temp. Mater. Processes* **1996**, *15*, 117.
[3] F. Thevenot, *J. Eur. Ceram. Soc.* **1990**, *6*, 205.
[4] D. K. Bose, K. U. Nair, C. K. Gupta, *High Temp. Mater. Processes* **1986**, *7*, 133.

[5] C. F. Bilsby, A. M. T. Bell, F. W. Morris, *Swelling of Boron Carbide Under Fast Neutron Irradiation*, IOP Publishing, Bristol, UK **1990**.
[6] R. J. K. Wood, D. W. Wheeler, D. C. Lejeau, B. G. Mellor, *Wear* **1999**, *233-235*, 134.
[7] E. Amberger, W. Stumpf, K. C. Buschbeck, *Gmelin Handbook of Inorganic Chemistry*, Springer-Verlag, Berlin **1981**.
[8] K. A. Schwetz, A. Lipp, *Ullmann's Encyclopedia of Industrial Chemistry*, (Ed: E. W. E. Gerhartz), VCH, Weinheim **1985**, p. 295.
[9] M. Beauvy, *J. Less-Common Metals* **1983**, *90*, 169.
[10] J. C. Oliveira, O. Conde, *Thin Solid Films* **1997**, *307*, 29.
[11] T. S. Moss, W. J. Lackey, K. L. Moore, *J. Am. Ceram. Soc.* **1998**, *81*, 3077.
[12] K. Ploog, *J. Cryst. Growth* **1974**, *24*, 197.
[13] A. O. Sezer, J. I. Brand, *Mater. Sci. Eng.* **2001**, *B79*, 191.
[14] G. M. Blumenstock, R. A. M. Keski-Kuha, *Appl. Opt.* **1994**, *33*, 5962.
[15] S. Lee, J. Mazurowski, G. Ramseyer, P. A. Dowben, *J. Appl. Phys.* **1992**, *72*, 4925.
[16] D. Zhang, B. G. Kempton, D. N. McIloy, Y. Geng, M. G. Norton, *Mater. Res. Soc. Proc.* **1999**, *536*, 323.
[17] S. Mondal, A. K. Banthia, *J. Eur. Ceram. Soc.* **2005**, *25*, 287.
[18] S. Lartigue, D. Cazajous, M. Nadal, G. Male, *Proc. Euro CVD* **1985**, *5*, 413.
[19] Y. Liu, L. Zhang, L. Cheng, Q. Zeng, W. Zhang, W. Yang, Z. Feng, S. Li, B. Zeng, *Appl. Surf. Sci.* **2009**, *255*, 5729.
[20] S. Veprek, *J. Nucl. Mater.* **1989**, *162-164*, 724.
[21] H. Kuenzli, P. Gartenbein, R. Steiner, P. Oelhafen, *J. Nucl. Mater.* **1992**, *196-198*, 622.
[22] K. Kourtakis, *USA Patent* 7556788, **2009**.
[23] T. T. Xu, J.-G. Zheng, N. Wu, A. W. Nicholls, J. R. Roth, D. A. Dikin, R. S. Ruoff, *Nano Lett.* **2004**, *4*, 963.
[24] E. Wiberg, N. Wiberg, A. F. Holleman, *Inorganic Chemistry*, Academic Press, San Diego, CA **2001**.
[25] K. J. Ganesh, M. Kawasaki, J. P. Zhou, P. J. Ferreira, paper presented at the *Microscopy and Microanalysis* conference, Richmond, VA, July 30 **2009**.
[26] K. J. Ganesh, M. Kawasaki, J. P. Zhou, P. J. Ferreira, unpublished.
[27] P. Rogl, *Phase Diagrams of Ternary Metal-Boron-Carbon Systems*, ASM International, Stuttgart, Germany **1998**.
[28] K. Ploog, M. Druminski, *Krist. Tech.* **1974**, *9*, 25.
[29] M. M. Ennaceur, B. Terreault, *J. Nucl. Mater.* **2000**, *280*, 33.
[30] C. Ronning, D. Schwen, S. Eyhusen, U. Vetter, H. Hofsass, *Surf. Coat. Technol.* **2002**, *158*, 382.
[31] J. Moulder, W. Stickle, P. Sobel, E. Bomben, *Handbook of X-Ray Photoelectron Spectroscopy*, Physical Electronics, Eden Prairie, MN **1995**.
[32] J. Lawrence, E. Zelonople, W. V. Hough, *USA Patent* 3 281 218, **1969**.
[33] J. C. Vickerman, *Surface Analysis-The Principle Techniques*, John Wiley & Sons, Chichester, UK **1997**.
[34] Y. N. Xia, P. D. Yang, Y. G. Sun, Y. Y. Wu, B. Mayers, B. Gates, Y. D. Yin, F. Kim, Y. Q. Yan, *Adv. Mater.* **2003**, *15*, 353.
[35] B. Li-Hong, L. Chen, T. Yuan, T. Ji-Fa, H. Chao, W. Xing-Jun, S. Cheng-Min, G. Hong-Jun, *Chin. Phys. B* **2008**, *17*, 1674.
[36] R. S. Wagner, W. C. T. Ellis, *Metall. Soc. AIME* **1965**, *233*, 1053.
[37] C. M. Lieber, *Solid State Commun.* **1998**, *107*, 106.
[38] J. Hu, T. W. Odom, C. M. Lieber, *Acc. Chem. Res.* **1999**, *32*, 435.
[39] N. N. Greenwood, A. Earnshaw, *Chemistry of the Elements*, Reed Educational and Professional Publishing Ltd., Oxford, UK **1997**.
[40] D. M. Matheu, A. M. Dean, J. M. Grenda, W. H. Green, *J. Phys. Chem. A* **2003**, *107*, 8552.
[41] A. Holmer, O. Olsvik, O. A. Rokstad, *Fuel Processing Technol.* **1995**, *42*, 249.
[42] V. R. Choudhary, A. M. Rajput, B. Prabhakar, *Catal. Lett.* **1995**, *32*, 391.
[43] H. G. Weiss, I. Shapiro, *J. Am. Chem. Soc.* **1953**, *75*, 1221.
[44] Y. Kwano, T. Fukuda, T. Kawarada, I. Mochida, Y. Korai, *Carbon* **1999**, *37*, 555.